11th International Symposium on Turbulence and Shear Flow Phenomena (TSFP11)
Southampton, UK, July 30 to August 2, 2019

DNS STUDY OF TURBULENT FLOW AND HEAT TRANSFER IN A SQUARE DUCT WITH TRANSVERSE RIBS

Bing-Chen Wang
Department of Mechanical Engineering
University of Manitoba
Winnipeg, MB, R3T 5V6, Canada
BingChen.Wang@umanitoba.ca

S. Vahid Mahmoodi J.
Department of Mechanical Engineering
University of Manitoba
Winnipeg, MB, R3T 5V6, Canada
mahmoosv@myumanitoba.ca

ABSTRACT

Turbulent flow structures and heat transfer in a ribbed square duct of different blockage ratios ($Br = 0.05$, 0.1 and 0.2) are investigated using direct numerical simulation (DNS). It is observed that the secondary flow structures intensely interact with the rib elements and boundary layers developed over the four sidewalls of the duct, which has a significant impact on the distribution of Nusselt number and subsequently gives rise to heat transfer enhancement on the smooth walls of the duct. It is also found that the distribution of drag and its influence on heat transfer and mixing are highly sensitive to the rib height. The impacts of rib height on turbulent coherent structures and heat transfer are investigated using vortex swirling strengths, joint probability density functions (JPDF) between the temperature and velocity fluctuations, statistical moments of different orders, and temperature spectra.

INTRODUCTION

Turbulent heat and fluid flows in a closed duct feature interactions of four boundary layers developed over the sidewalls of a square duct. In addition, wall-mounted rib elements further generate strong disturbances and facilitate large-scale secondary flows which dynamically interact with the four momentum and thermal boundary layers. Rib roughened surface in a low aspect ratio duct can enhance the momentum and heat transfer, and is frequently employed in industrial applications, such as turbine blade cooling and heat exchangers. Nagano *et al.* (2004) conducted DNS of a fully-developed turbulent channel flow to investigate the effects of transverse rib roughness elements on both the velocity and temperature fields. Their results showed that k-type roughness has the best heat transfer performance due to the promotion of turbulent mixing in regions downstream of ribs. Leonardi *et al.* (2015) also studied the effects of pitch-to-height ratios (P/H) and rib shapes on the heat transfer enhancement in a turbulent channel flow. They found that turbulent heat flux reaches its maximum level at $P/H = 7.5$ for both square and circle ribs. Here P and H denote the spacing between the ribs and the rib height, respectively. Liou *et al.* (1993) conducted LDV measurement for fully-developed channel flow with square ribs mounted on the top and bottom walls. They observed that due to the mean secondary flow, the impingement region on the sidewall resulted in high heat transfer rates. Ooi *et al.* (2002) studied turbulent flow and heat transfer using the Reynolds-averaged Navier-Stokes (RANS) method. They reported that the occurrence of secondary flows significantly alters the temperature field, which consequently leads to a heat transfer enhancement.

Notwithstanding the aforementioned contributions, the number of detailed studies of turbulent heat and flows in a closed low-aspect-ratio duct is still limited. In view of this, we conduct a comparative DNS study of rib-roughened duct flow and heat transfer. The objective of this research is to investigate the mechanism underlying the organized secondary flows and their effects on turbulent heat transfer and coherent structures in both physical and spectral spaces.

TEST CASE AND NUMERICAL ALGORITHM

The length of the square duct is $6.4D$ long and consists of eight rib periods, where D is the hydraulic diameter. In the current computation, three blockage ratios ($Br = 0.05$, 0.1 and 0.2) are compared, while the spacing between the ribs is kept constant at $P = 0.8D$. The flow field is fully developed, and periodic boundary conditions are applied to the streamwise direction. No-slip boundary condition is imposed on all solid walls for the velocity field. Reynolds number is fixed at $Re_b = U_b\delta/\upsilon = 2800$, where U_b denotes the streamwise bulk mean velocity and $\delta = 0.5D$ is half side length of the square duct. For the temperature field, it is assumed that the air enters the duct at an inlet temperature, $T_{in} = 300K$. The Prandtl number of the air is $Pr = 0.71$. The temperature of the heated wall and ribs is maintained constant at $T_{wall} = 350K$ while the sidewalls are assumed to be adiabatic. The temperature field is treated as a passive scalar and is non-dimensionalized using the inlet and bottom temperature difference, i.e. $\theta = (T - T_{in})/(T_w - T_{in})$.

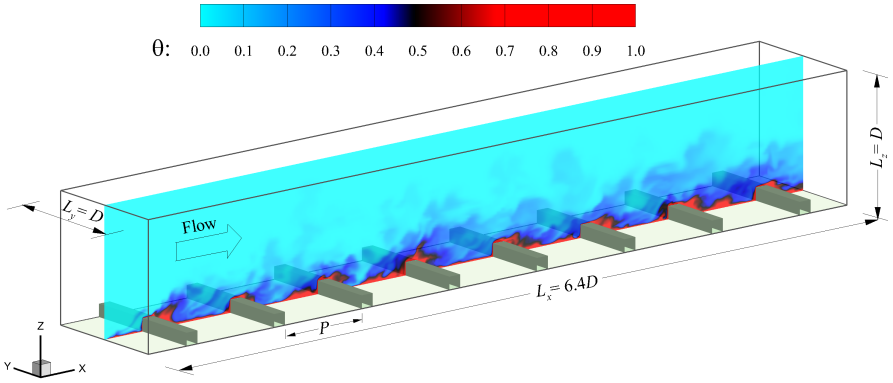

Figure 1: Schematic of a square duct with transverse ribs and coordinate system. Contours of instantaneous non-dimensional temperature are displayed in the central plane (located at $y/\delta = 0.0$) of the entire domain.

The continuity, momentum and thermal energy equations based on a generalized curvilinear coordinate system (ξ_1, ξ_2, ξ_3) for an incompressible flow are written as

$$\frac{1}{J}\frac{\partial\left(\beta_i^k u_i\right)}{\partial \xi_k} = 0 \quad , \tag{1}$$

$$\frac{\partial u_i}{\partial t} + \frac{1}{J}\frac{\partial}{\partial \xi_k}\left(\beta_j^k u_i u_j\right) = -\frac{1}{J\rho}\frac{\partial\left(\beta_i^k p\right)}{\partial \xi_k} - \frac{1}{\rho}\Pi\delta_{1i} + \frac{\nu}{J}\frac{\partial}{\partial \xi_p}\left(\frac{1}{J}\beta_j^p \beta_j^q \frac{\partial u_i}{\partial \xi_q}\right) \quad , \tag{2}$$

$$\frac{\partial T}{\partial t} + \frac{1}{J}\frac{\partial}{\partial \xi_k}\left(\beta_j^k T u_j\right) = \frac{\alpha}{J}\frac{\partial}{\partial \xi_p}\left(\frac{1}{J}\beta_j^p \beta_j^q \frac{\partial T}{\partial \xi_q}\right) \quad , \tag{3}$$

where u_i, p, T, ν, ρ, α and δ_{ij} represent the velocity, pressure, temperature, kinematic viscosity, density, thermal diffusivity, and Kronecker delta, respectively, and Π denotes a constant streamwise pressure gradient that drives the flow. Also, β_i^j and J denote the cofactor and Jocobian of tensor $\partial x_i/\partial \xi_j$, respectively. The above governing equations are represented using tensor notations, and the streamwise (x), wall-normal (z), and spanwise (y) coordinates shown in Fig. 1 are also denoted using x_i for $i = 1, 2$, and 3, respectively.

DNS is performed based on an in-house computer code developed using the FORTRAN 90/95 programming language and parallelized following the message passing interface (MPI) standard. The numerical algorithm is based on a finite-volume method in which a second-order accuracy is achieved with respect to both spatial and temporal discretizations. Within each sub-step of the second-order Runge-Kutta scheme, a fractional-step method is applied and a pressure correction equation is solved using the parallel algebraic multigrid solver. For time advancement, the Courant-Friedrichs-Lewy (CFL) number is approximately 0.2. To ensure the numerical accuracy demanded by DNS, the simulations are conducted based on $1280 \times 152 \times 148$ grid points, such that the grid resolution strictly follows $\eta < \Delta_{\max} < 5\eta$, where η is the Kolmogorov scale and $\Delta_{\max}$ is the maximum grid size. All the simulations were conducted using the WestGrid (Western Canada Research Grid) supercomputers. For each simulated case, approximately 548,000 CPU hours were spent on solving the velocity and temperature fields and for collecting the flow statistics.

RESULTS AND DISCUSSIONS

Figure 2 shows the contours of the mean temperature superimposed with in-plane streamlines in the central plane for the studied blockage ratios. There is a recirculation bubble between two ribs, with its center located at "point II" in the streamwise direction. Clearly, the recirculation bubble becomes increasingly elongated with an increasing rib height. This phenomenon inevitably has an impact on both the local drag and heat transfer. Owing to the existence of the small velocity (roughly 15% of the free-stream velocity) within the recirculation zone, a strong adverse pressure gradient is induced, further causing the flow to reattach onto the bottom wall. It is reported (Vogel & Eaton, 1985) that the local heat transfer coefficient reaches its maximum value upstream of the reattachment point (i.e., point III). By comparing Figs. 2(a)−2(c), it is clear that the corner vortex (point I) is not observed at $Br = 0.05$ due to the fact that the rib height is not great enough to cause a significant sudden expansion of the flow in the lee of the rib. However, the size of the corner vortex increases as the rib height increases. Downstream of the reattachment point, a new boundary layer starts to build up and impinges onto the next rib which leads to the generation of an upstream vortex (at point IV). Vertical motion of this type of vortex forces cold mainstream towards the ribbed wall thereby affecting the heat transfer performance.

To assess the effects of the blockage ratio on the temperature field, the non-dimensional temperature profiles at four streamwise locations are plotted in Fig. 3. These profiles show a drop in temperature gradient values with an increasing streamwise distance from the inlet ($x/\delta = 0$). Furthermore, it is observed that in all three rib cases, six rib periods are required for the temperature field to reach the fully-developed condition. As shown in Figs. 3(a)−3(c), the mean temperature gradient becomes zero as the smooth top wall is approached due to the prescribed adiabatic condition. This figure clearly indicates that the mean temperature increases monotonically as the streamwise distance (x/δ) increases, reflecting the fact that the flow is continuously heated by the ribbed wall. Furthermore, owing to the presence of rib, the mean temperature enhances drastically around the rib crest.

In order to investigate the effects of the secondary flow structures on heat transfer, the strength of the secondary flow must be quantized. In doing so, the mean spanwise-vertical velocity $S = \sqrt{(\langle w\rangle^2 + \langle v\rangle^2)/(\langle u\rangle^2 + \langle w\rangle^2 + \langle v\rangle^2)}$ is considered, where $\langle u\rangle$, $\langle w\rangle$, and $\langle v\rangle$ represent time-

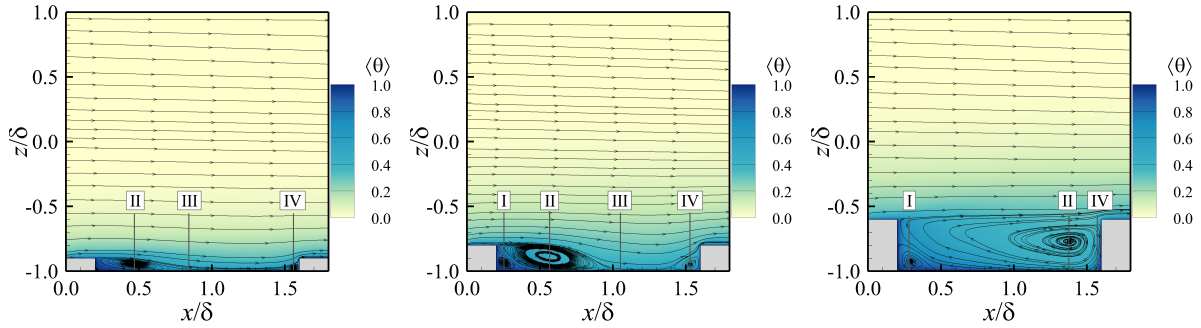

(a) $Br = 0.05$ (b) $Br = 0.1$ (c) $Br = 0.2$

Figure 2: Contours of the mean temperature superimposed with in-plane streamlines in the central x-z plane (located at $y/\delta = 0.0$) for different blockage ratios.

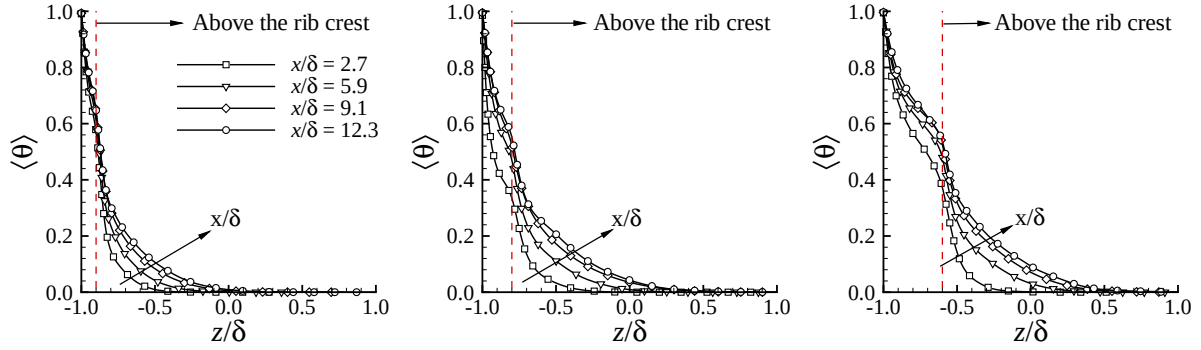

(a) $Br = 0.05$ (b) $Br = 0.1$ (c) $Br = 0.2$

Figure 3: Comparison of the normalized mean temperature profiles at four streamwise locations in the central plane (located at $y/\delta = 0.0$) for different blockage ratios.

averaged velocity in the streamwise, vertical, and spanwise directions, respectively. Figure 4 shows secondary flow vectors and contours of S in a plane normal to the streamwise direction for each rib case. From this figure, it is clear that the secondary flow structures are mainly responsible for transporting the relatively cooler fluid from the center of the duct to the bottom wall, giving rise to a region with high Nu values. It is also observed that the secondary flow strength is very intense in the vicinity of the rib crest. From Figs. 4(a)−4(c), it is interesting to observe that the impingement region towards the sidewalls becomes increasingly elevated from the bottom wall as the rib height increases. This phenomenon prevents cold fluid from contacting the heated wall and thus lowers the heat transfer rate at the bottom wall within the recirculation zone.

To understand the impact of secondary flow structures on heat transfer, the distribution of Nu is shown in Fig. 5. The Nusselt number is defined as $Nu = q_w D/\lambda(T_w - T_b)$, where the bulk temperature is calculated as $T_b = \int_0^D \int_0^D \int_0^{L_x} T|U|dxdzdy \Big/ \int_0^D \int_0^D \int_0^{L_x} |U|dxdzdy$. In this comparative study, Nu is further divided by the value calculated using the Dittus-Boelter equation, i.e. $Nu_0 = 0.023 Re^{0.8} Pr^{0.4}$. As seen in Fig. 5, mean secondary flow structures significantly influence the spatial distribution of Nu on the bottom wall. From this figure, it is also clear that the value of Nu on the windward side of the rib is larger in case of $Br = 0.2$ than in cases of $Br = 0.05$ and $Br = 0.1$. This is because the recirculation zone (see, Fig. 2) induces a large positively valued pressure on the windward face of the rib, thereby enhancing the mixing and heat transfer rate in that region. Furthermore, as a result of the developing temperature field (in conjunction with a fully-developed turbulent flow field), the Nusselt number decays streamwise until the temperature field reaches a fully-developed state. It is also observed that the local Nusselt number contour pattern becomes similar after the sixth rib, which indicates a quasi self-similar state.

To further investigate the effects of the mean flow field on the heat transfer distribution, Fig. 6 compares the streamwise profiles of the total drag, $C_f + C_p$, and Nusselt number, Nu/Nu_0, at $(y/\delta, z/\delta)$=(0.0, -1.0) in the central x-z plane for the three different rib cases. The skin friction and form drags are defined as $C_f = \tau_w/(\rho U_b^2/2)$ and $C_p = \langle p \rangle / \left(\frac{1}{2}\rho U_b^2\right)$, respectively, where τ_w represents the local total wall friction stress calculated as $\tau_w = \mu \left[(\partial \langle u \rangle / \partial z)^2 + (\partial \langle v \rangle / \partial z)^2 \right]^{1/2}_{y=0}$. As seen in Fig. 6(a), for all three rib cases, the level of total drag near the windward face of the rib increases monotonically as the rib height increases. This is evident from Fig. 2, which shows that the size and strength of the recirculation region (point II) increase when the rib height is augmented; and as a result, a higher magnitude of drag is observed in that region. Fig. 6(b) highlights the fact that the temperature field and heat transfer rate respond differently to the mean flow structure patterns. For example, in the region downstream of the rib, the peak of Nu lies at the reattachment point (point II) and immediately upstream of the rib (point IV) for the cases of $Br = 0.05$ and $Br = 0.1$, while for $Br = 0.2$, a sole peak is situated at the latter position (point IV). This leads to the conclusion that at a sufficiently high Br value, the reattachment point occurs at the windward face of the following rib element, giving rise to not only an augmentation of the stag-

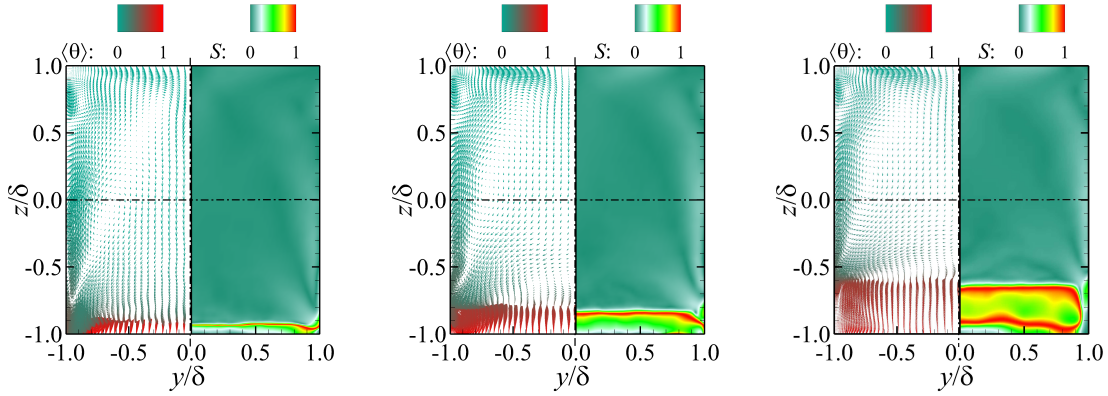

(a) $Br = 0.05$ (b) $Br = 0.1$ (c) $Br = 0.2$

Figure 4: Mean secondary flow vectors and secondary flow strength S at position $x/\delta = 9.1$ for different rib cases.

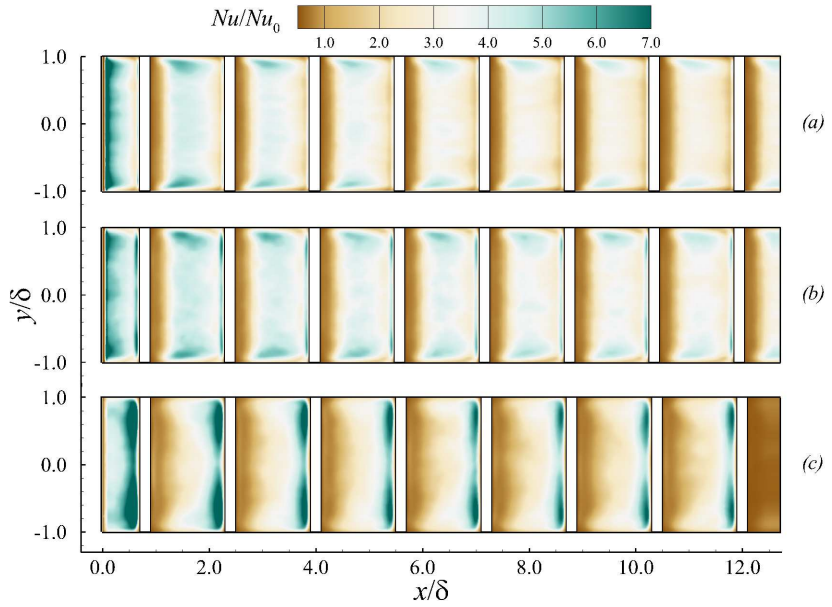

Figure 5: Distribution of the local Nusselt number on the bottom wall located at $z/\delta = -1.0$ for different rib cases. (a) $Br = 0.05$, (b) $Br = 0.1$, and (c) $Br = 0.2$.

nation pressure but also an amplified magnitude of Nu.

Figures 7(a) and 7(b) show the vertical profiles of TKE ($\langle k \rangle = \langle u_i' u_i' \rangle / 2$) and temperature variance $\langle \theta' \theta' \rangle$ for different blockage ratios along a central vertical line located at $(x/\delta, y/\delta)$=(9.1, 0.0), respectively. From Fig. 7(a), it is clear that owing to the presence of a strong shear layer, the value of the turbulent intensity progressively increases with the increase of rib height in the region immediately above the rib crest. However, in contrast to this trend of the turbulent intensity, the value of temperature variance decreases as the rib height increases in that region. These opposite trends of the TKE and temperature variance can be explained through an investigation of the rib height effect on the production term, $P_{j\theta} = -\langle u_j' \theta' \rangle \partial \langle \theta \rangle / \partial x_j$, of the transport equation of the temperature variance. As is clear in Fig. 7(c), similar to the trend of $\langle \theta' \theta' \rangle$, the total production term, $P_t = P_{1\theta} + P_{2\theta} + P_{3\theta}$, increases monotonically as the blockage ratio decreases near the rib crest. This is because the vertical gradient of the mean temperature, $\partial \langle \theta \rangle / \partial z$, makes a considerable contribution to the production term in the region close to the ribbed bottom wall for $-1.0 < z/\delta < -0.9$ (see, Fig. 3), which results in an increase in the magnitude of $P_{j\theta}$ with a decreasing rib height. This observation is fully consistent with the results obtained by Nagano *et al.* (2004) in the sense that the low level of temperature variance is attributed to high blockage ratios.

Figure 8 shows the vertical profiles of the mean Reynolds shear stress, $\langle u' w' \rangle$, and mean axial and normal turbulent heat fluxes, $\langle u' \theta' \rangle$ and $\langle w' \theta' \rangle$, for different blockage ratios at the same location as in Fig. 7. These profiles exhibit the same trend as is observed in the turbulent intensity, highlighting the fact that the wall-mounted rib elements impose a strong disturbance near the ribbed bottom wall, leading to an increase in the Reynolds shear stress and both the axial and normal turbulent heat fluxes in the region immediately above the rib crest.

In order to study the effects of fluid motions (ejections and sweeps) on turbulent heat transfer near the ribbed rough wall, joint probability density functions (JPDF) of $\sigma_u = u'/u_{rms}$, $\sigma_w = w'/w_{rms}$, and $\sigma_\theta = \theta'/\theta_{rms}$ are calculated for the rib case with $Br = 0.1$ at the location $(x/\delta, z/\delta)$= (9.1, -0.76), where the peaks of the three components $\langle \theta' \theta' \rangle$, $\langle u' \theta' \rangle$, and $\langle w' \theta' \rangle$ are situated. Figures 9(a) and 9(b) show that there exists a strong negative correlation between u' and θ', and a positive correlation between w' and θ', respectively. The thick black dash line at 45° indicates a high

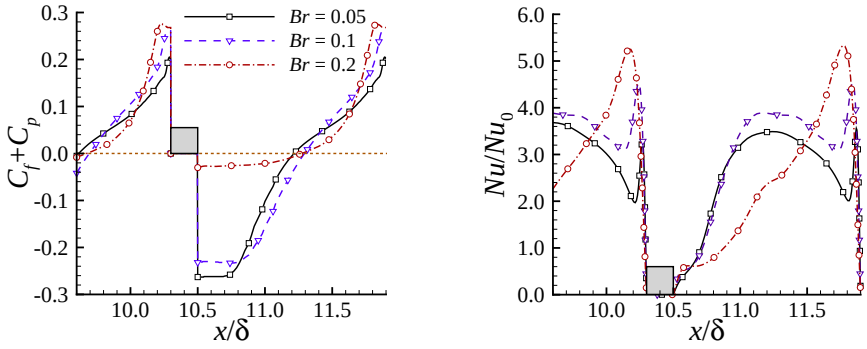

(a) Profiles of $C_f + C_p$ (b) Profiles of Nu/Nu_0

Figure 6: Streamwise profiles of non-dimensionalized total drag $C_f + C_p$ and Nusselt number Nu/Nu_0 of different blockage ratios along a central vertical line located at $(y/\delta, z/\delta)$=(0.0, -1.0).

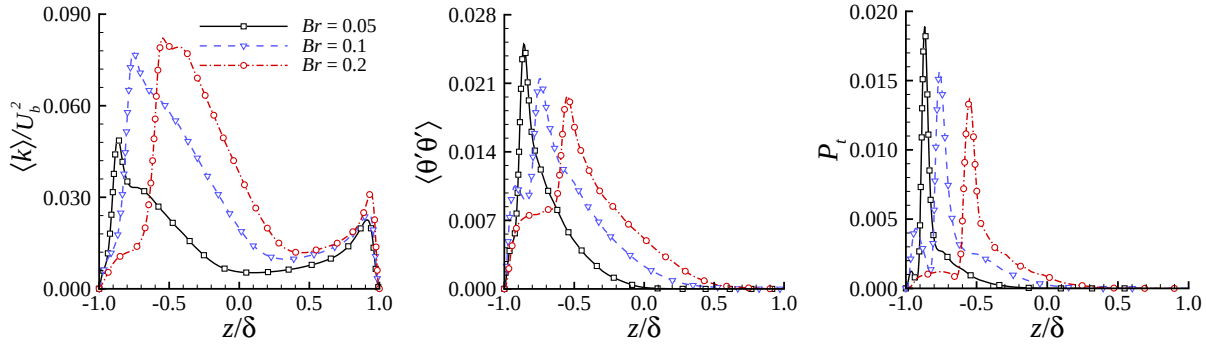

(a) Profiles of $\langle K \rangle$ (b) Profiles of $\langle \theta'\theta' \rangle$ (c) Profiles of P_t

Figure 7: Vertical profiles of non-dimensionalized TKE $\langle k \rangle$, temperature variance $\langle \theta'\theta' \rangle$, and production P_t term of different blockage ratios along a central vertical line located at $(x/\delta, y/\delta) = (9.1, 0.0)$.

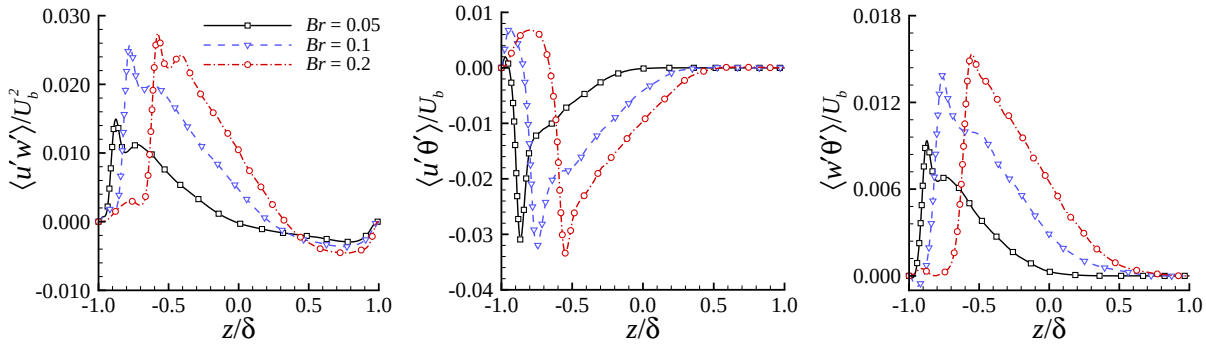

(a) Profiles of $\langle u'w' \rangle$ (b) Profiles of $\langle u'\theta' \rangle$ (c) Profiles of $\langle w'\theta' \rangle$

Figure 8: Vertical profiles of non-dimensionalized Reynolds shear stress $\langle u'w' \rangle$ and turbulent heat fluxes $\langle u'\theta' \rangle$ and $\langle w'\theta' \rangle$ of different blockage ratios along a central vertical line located at $(x/\delta, y/\delta) = (9.1, 0.0)$.

correlation between components at the reference point. For the JPDF between σ_θ and σ_u, quadrant distribution shows that the second (Q_2) and fourth (Q_4) events are dominant in frequency of occurrence, which corresponds to the negative values of $\langle u'\theta' \rangle$ near the rib crest shown in Fig. 8(b). In contrast, the JPDF of σ_θ and σ_w shows a tendency towards the first (Q_1) and third (Q_3) events leading to positively-valued $\langle w'\theta' \rangle$ in Fig. 8(c). The obtained results of the JPDF analysis at this reference point indicate that the sweep and ejection events are dominant near the rib crest, which is mainly attributed to the large-scale flapping motions in this region.

Figure 10 compares the pre-multiplied spectra of the non-dimensional temperature at different wall-normal locations for the rib case of $Br = 0.1$. Note that the pre-multiplied spectra $(fE_{\theta\theta})$ of temperature fluctuations is non-dimensionalized using the bulk and inlet temperature difference, i.e. $\theta_d = (T_b - T_{in})$. It is evident from Fig. 10 that owing to the presence of the energetic vortices near the rib crest, the temperature at $z/\delta = -0.76$ fluctuates with a larger magnitude and a lower primary frequency compared to that of the other two positions near the core regions of the duct. This observation confirms that the energy spectrum is largely influenced by the vortex shedding events over the rib crest, as the magnitude of $fE_{\theta\theta}$ is significantly higher in the region immediately above the rib crest.

Figure 11 shows the iso-surfaces of the swirling strength, λ_{ci}, superimposed onto instantaneous temperature contours in the central plane of the domain for two differ-

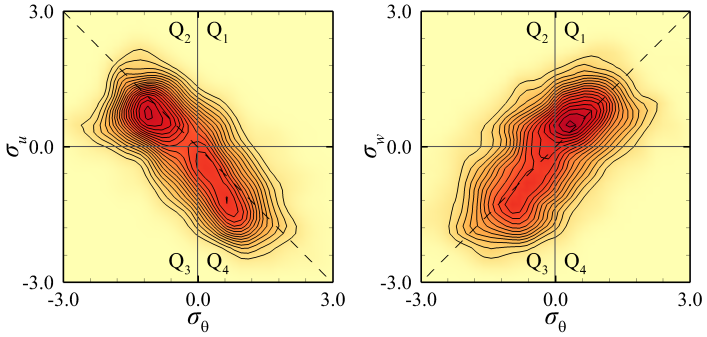

(a) JPDF of σ_θ and σ_u (b) JPDF of σ_θ and σ_w

Figure 9: JPDF of σ_θ, σ_u and σ_w at the location $(x/\delta, z/\delta)$= (9.1, -0.76) for the rib case of $Br = 0.1$. Contours are plotted with an incremental JPDF value of 0.0035.

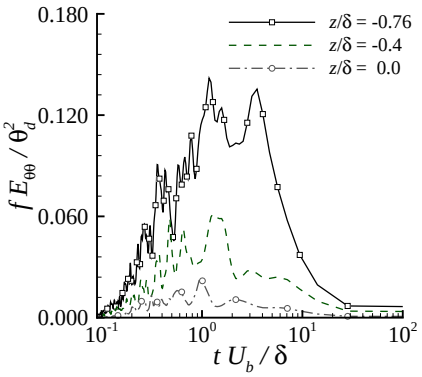

Figure 10: Pre-multiplied temperature spectra $fE_{\theta\theta}$ for $Br = 0.1$ at position x/δ=9.1 for different vertical locations.

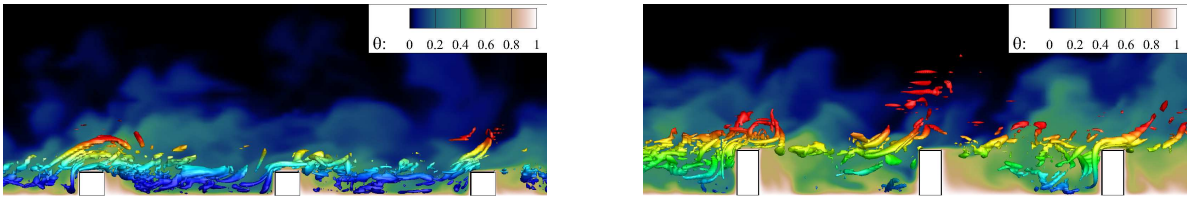

(a) $Br = 0.1$ (b) $Br = 0.2$

Figure 11: Iso-surfaces of the swirling strength λ_{ci} around ribs, colored with z/δ, with background instantaneous temperature in the central plane (located at $y/\delta = 0$) of the domain for two different rib cases of $Br = 0.1$ and 0.2.

ent rib cases. It is interesting to observe that an increase of the rib height induces significant changes in the dynamics of turbulence structures near the ribbed bottom wall. These changes are characterized by the stretching and shedding of vortices in the region above the rib crest, leading to an enhanced strength of the turbulent motions (as indicated by the magnitude of TKE in Fig. 7(a)) and amplified heat transfer rates in that region. Furthermore, it is observed that an increased rib height is accompanied by an augmentation of upward turbulent motion at the leading edge of the rib element, which gives rise to a lifting of the turbulence structures, and consequently, enhancement of the local turbulent heat flux as shown previously in Fig. 8(c).

CONCLUSIONS

Direct numeric simulation is performed for ribbed square duct flows of various blockage ratios to investigate the effect of three-dimensional secondary flow structures on heat transfer enhancement. Results show that the difference in the pattern of mean flow structures on both leeward and windward surfaces of a rib causes a variation in Nusselt number distribution. For instance, in the case of $Br = 0.2$, the size of the corner vortex becomes larger which causes a decrease in the heat transfer rate. It is also observed that the secondary flow significantly affects the gradient and distribution of Nusselt number close to the sidewalls, where the local heat transfer rate decreases with an increasing rib height. Furthermore, it is discovered that as the rib height increases in the region near the rib crest, both the streamwise and vertical turbulent heat fluxes (i.e., $\langle u'\theta'\rangle$ and $\langle w'\theta'\rangle$, respectively) are enhanced, whereas the temperature variance, $\langle\theta'\theta'\rangle$, decreases monotonically. By investigating the production term in the transport equation of the temperature variance $\langle\theta'\theta'\rangle$, it is concluded that the magnitude of the mean vertical temperature gradient increases significantly near the rib crest as the rib height decreases, leading to an augmentation of the magnitude of turbulent production term, P_t, in that region. In consequence, the magnitude of the temperature variance, $\langle\theta'\theta'\rangle$, becomes greater near the rib crest as the blockage ratio decreases.

The investigations of turbulent structures along with instantaneous temperature indicate that, owing to the significant disturbances generated by the rib elements, the vortical structures near the bottom wall are drastically deflected. This leads to the formation of incoherent structures and the generation of several violent ejection and sweep motions just above the rib elements, which further lead to an increase of local turbulent heat flux.

REFERENCES

Leonardi, S., Orlandi, P., Djenidi, L. & Antonia, R. A. 2015 Heat transfer in a turbulent channel flow with square bars or circular rods on one wall. *J. Fluid Mech.* **776**, 512–530.

Liou, T. M., Wu, Y. Y. & Chang, Y. 1993 LDV measurements of periodic fully developed main and secondary flows in a channel with rib-disturbed walls. *J. Fluids Eng.* **115**, 109–114.

Nagano, Y., Hattori, H. & Houra, T. 2004 DNS of velocity and thermal fields in turbulent channel flow with transverse-rib roughness. *Int. J. Heat Fluid Flow* **25**, 393–403.

Ooi, A., Iaccarino, G., Durbin, P. A. & Behnia, M. 2002 Reynolds averaged simulation of flow and heat transfer in ribbed ducts. *Int. J. Heat Fluid Flow* **23**, 750–757.

Vogel, J. C. & Eaton, J. K. 1985 Combined heat transfer and fluid dynamic measurements downstream of a backward-facing step. *J. Heat Trans.* **107**, 922–929.